IVYSPRING INTERNATIONAL PUBLISHER

Theranostics

2019; 9(13): 3866-3878. doi: 10.7150/thno.31864

Research Paper

Polydopamine coated multifunctional lanthanide theranostic agent for vascular malformation and tumor vessel imaging beyond 1500 nm and imaging-guided photothermal therapy

Xiaolong Li, Mingyang Jiang, Songjun Zeng✉ and Hongrong Liu✉

School of Physics and Electronics and Key Laboratory of Low-dimensional Quantum Structures and Quantum Control of the Ministry of Education, Synergetic Innovation Center for Quantum Effects and Applications, Hunan Normal University, Changsha, Hunan 410081 (China)

✉ Corresponding authors: songjunz@hunnu.edu.cn; hrliu@hunnu.edu.cn

Received: 2018.11.28; Accepted: 2019.03.25; Published: 2019.05.31

Abstract

The optical imaging guided tumor vessels and vascular malformation visualization by using the second near infrared emission beyond 1500 nm (NIR-II) is emerged as the next generation fluorescence imaging technique for early tumor diagnosis and identification of tumor-associated vascular features. On the other hand, developing theranostic probes for NIR-II imaging guided photothermal therapy (PTT) is of great significance, which is rarely explored. Herein, a high performance theranostic nanoplatform based on the core-shell structured $NaLuF_4$ nanorods@polydopamine (denoted as NRs@PDA) by integrating the new advanced NIR-II imaging beyond 1500 nm with PTT function was developed for tumor-associated vascular malformation visualization and imaging-guided PTT.

Methods: In this work, the hydrophilic $NaLuF_4$ NRs@PDA therapeutic probe was synthesized by using a reverse microemulsion method. The crystal phase, morphology, emission spectra and photothermal performance of the synthesized samples were systematically characterized. The NIR-II optical imaging and photothermal properties were investigated by *in vitro* and in *vivo* experiments.

Results: The $NaLuF_4$ NRs@PDA therapeutic probe possessed efficient NIR-II emission centered at 1525 nm with high quantum yield (QY), good photo-stability and high biocompatibility. *In vivo* NIR-IIb imaging based on the designed probe can clearly visualize the whole-body vessel and brain vessel with high spatial resolution, especially tumor-associated vessels. In addition, *in vitro* and *in vivo* experiments also demonstrated that the designed $NaLuF_4$ NRs@PDA probe possessed efficient photothermal conversion efficiency (40.18%) for PTT ablation of tumor.

Conclusion: With the excellent NIR-II imaging ability and PTT of tumor, the designed theranostic nanoplatform successfully realize the simultaneous tumor vessel diagnosis and tumor therapy, which may provide the opportunity of designing new theranostic bioprobes with combination of the NIR-II optical imaging technique and PTT function for tumor diagnosis and therapy.

Key words: Lanthanide nanorods; theranostic nanoplatform; tumor angiography; photothermal therapy

Introduction

Recently, multifunctional nanoprobes combined features of imaging and therapeutic functions have received considerable attention due to the rapid development of nanotechnology in biomedicine [1-11]. Among the general combination of imaging modalities (such as ultrasound imaging, magnetic

resonance imaging, and fluorescence imaging) with therapy techniques (for example, PTT, photodynamic therapy, and chemotherapy), integrating optical imaging with PTT into a single nanoprobe has drawn immense attention for higher diagnosis requirement and enhanced therapeutic efficacy [12-16]. Fluorescence imaging has provided a facile method to visualize complex biological processes at the molecular level and brain/tumor vascular [17, 18]. In comparison with the conventional visible/NIR-I imaging, the new developed NIR-II imaging by utilizing the emission light in 1000-1700 nm has been considered as the next generation optical imaging technique with remarkable improvement in imaging sensitivity, and time/spatial resolution, owing to the significantly decreased photon scattering losses [19-22]. Therefore, constructing NIR-II imaging-based nanotheranostic agent is significantly important.

So far, only a few fluorophores capable of emitting NIR-II luminescence, such as small organic fluorophores [23, 24], quantum dots (QDs) [25, 26], single-walled carbon nanotubes (SWNTs) [27, 28]. Unfortunately, these small organic molecules retain in body too short to accumulate in diseased organs and tumor region, impeding their further applications in tumor detection and *in vivo* long-term studies [29, 30]. Meanwhile, most of QDs composed of toxic elements, such as lead, mercury or arsenic [31-33], hindering their wide-spread application for *in vivo* bioimaging. Although, SWNTs have been developed as NIR-II imaging bioprobes, there are still several drawbacks, such as relatively low QY, uncontrollable size distributions (ranging from several to hundreds of nanometers), and broad-band emission peaks (>300 nm) [34, 35]. These shortcomings ultimately inhibit their further applications in NIR-II imaging and size-dependent biodistribution study. Therefore, it is emergent to design efficient NIR-II imaging agent with narrow emission, controllable size and high QY. Recently, the lanthanide-based nanomaterials have been regarded as indispensable platforms for optical bioimaging due to the low photo-bleaching, low biotoxicity and high QY, and well-controlled size distribution [36-38]. Therefore, development of lanthanide-based NIR-II imaging agent for theranostic nanoprobes is required.

On the other hand, PTT has been considered as a promising non-invasive therapy technology to current treatments of tumor [39-42]. And, among the various photothermal agents (such as gold nanostructures, copper sulfide nanoparticles, and so on) [43-46], PDA derived from natural substances is considered as more promising PTT agent owing to the advantages of excellent biocompatibility, good biodegradability, and high photothermal conversion efficiency [47-50]. Therefore, the development of efficient theranostic nanoprobe with combination of lanthanide-based NIR-II agent and PDA is extremely demanded.

Here, we have developed a core-shell structured $NaLuF_4$: Gd/Yb/Er NRs@PDA as the integrative theranostic platform. The real-time optical bioimaging and imaging guided tumor detection based on the NRs@PDA were investigated in detail. Meanwhile, the through-skull non-invasive brain and abdomen vessel imaging without craniotomy was performed. In addition, non-invasive tumor vascular imaging was achieved. Apart from the NIR-II optical imaging, these NRs@PDA nanoprobes also possess high photothermal conversion efficiency, outstanding antitumor effect and excellent biocompatibility.

Results and Discussion

Structure characterization and optical properties of $NaLuF_4$ NRs@PDA nanoprobes

Scheme 1 presents the development of the core-shell structured NRs@PDA nanoprobes for NIR-II optical bioimaging/imaging-guided PTT application. And the shape and structure of the NRs@PDA nanoprobes were first characterized by transmission electron microscopy (TEM). As demonstrated in **Figure 1A** and **1B**, the rod-like morphology with high monodispersity and uniform size (average width and length of about 20 x 130 nm) was obtained. The high resolution TEM (HR-TEM) image displayed that the synthesized $NaLuF_4$ NRs presented high crystalline nature (**Figure 1D**), and the d-spacing was measured to be about 1.93 Å, corresponding to the (210) lattice plane of the hexagonal phase $NaLuF_4$. After PDA coated (**Figure 1C**), a thin PDA shell was successfully grown on the surface of the $NaLuF_4$: Gd/Yb/Er NRs, indicating the formation of core-shell structure. And the scanning transmission electron microscope (STEM) image (**Figure 1E**) also demonstrated the presence of an uniform PDA outer shell (about 5 nm) on the surface of $NaLuF_4$ NRs, further validating the core-shell structure. **Figure 1G** shows the powder XRD of the synthesized NRs with and without PDA modification. As demonstrated, all of the characteristic diffraction peaks of NRs and NRs@PDA were matched well with the standard hexagonal phase structure (JCPDS: 16-0334). No other impurity peaks were detected, confirming the formation of the pure hexagonal phase structure. It should be noted that $NaLnF_4$ host usually possesses two crystal phases including cubic and hexagonal and doping Gd^{3+} into $NaLnF_4$ host has great influence on the crystal phase and size of $NaLnF_4$ host. To reveal this, a comparison experiment with/without doping Gd^{3+} was performed. As shown

in **Figure S1,** the as-prepared $NaLuF_4$: Yb/Er without doping Gd is composed of two typical structures including small cube and large rod. While doping 40% Gd, the sample only presents highly uniform rod-like structure. And the XRD analysis further demonstrates the as-prepared $NaLuF_4$: Gd/Yb/Er nanocrystals exhibit pure hexagonal phase structure, indicating the Gd doping induced phase transformation from cubic to hexagonal. Furthermore, the X-ray photoelectron spectroscopy (XPS) analysis was performed. As demonstrated in **Figure S2**, after surface modification with PDA, besides the detection signals of Na, Lu, Gd, Yb and F, a new N element signal was obviously detected in NRs@PDA sample, further verifying the presence of PDA. Moreover, the Fourier transform infrared (FTIR) spectroscopy analysis was performed. As shown in **Figure S3**, the characteristic peaks centered at 1577 cm^{-1} and 1496 cm^{-1} of PDA were detected, further confirming the successful attachment of PDA on the surface of $NaLuF_4$ NRs.

To reveal the effect of PDA on the optical properties of NRs, the upconversion (UC) and downconversion (DC, NIR-II region) spectra of the both $NaLuF_4$ NRs and NRs@PDA excited by the 980 nm laser were studied. As demonstrated in **Figure 1H**, after successful encapsulation of the PDA shell on NRs, the intensity of both green/red UC and NIR-II DC emission is decreased, which is mainly ascribed to the efficient fluorescence resonance energy transfer (FRET) from NRs to PDA owing to the overlap between the absorption band of PDA and the emission peaks of NRs [41, 42]. However, it is worth noting that the red and NIR-II emissions of NRs@PDA are still strong, which fall in the "optical transparency window" with deeper penetration for excellent optical bioimaging. The green emission centered at 521/540 nm and the red emission centered at 650 nm were originated from the excited states $^2H_{11/2}$, $^4S_{3/2}$, and $^4F_{9/2}$ to ground state $^4I_{15/2}$ transition of Er^{3+}, respectively (**Figure 1F**). The NIR-II emission at 1525 nm was ascribed to the electron transition from $^4I_{13/2}$ to $^4I_{15/2}$ of Er^{3+} [51]. The NIR-II fluorescence QY of NRs@PDA in water was measured to be about 1.37 % using a standard IR-26 dye as reference (**Figure S4**), which was higher than that of SWNTs (0.1~0.4 %) probes [52, 53]. Moreover, the photo-stability curve and *in vitro* phantom bioimaging (**Figure S5**) were performed, revealing the superior photo-stability of $NaLuF_4$ NRs@PDA with a low photobleaching degree (0.96%) after 60 min irradiation, which was significantly lower than the previously reported small molecular probe [29]. Additionally, compared with the indocyanine green (ICG), the synthesized NRs@PDA also presents superior photo-stability (**Figure S6**). Therefore, it is expected that the NRs@PDA nanocomposites are promising probe for *in vivo* NIR-II optical bioimaging with high sensitivity.

NIR-II imaging-guided tumor vessel tracking

Prior to *in vivo* NIR-II bioimaging, the cytotoxicity of $NaLuF_4$ NRs@PDA was evaluated by 3-(4, 5-dimethylthiazol-2-yl)-2-5-diphenyl-tetrazolium bromide (MTT) assay. As demonstrated in **Figure S7**,

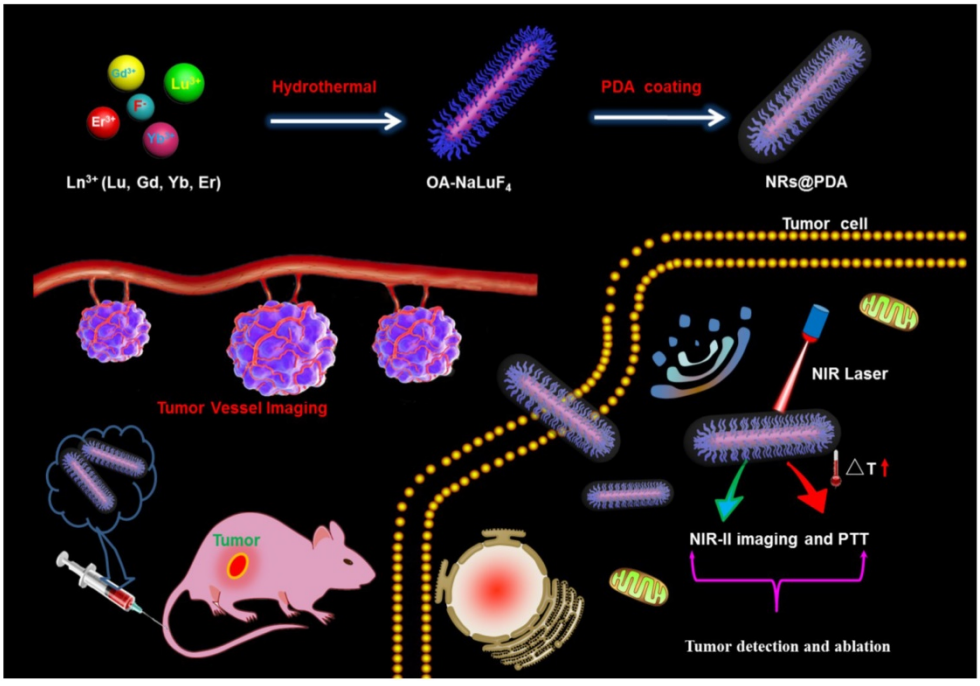

Scheme 1. Schematic illustration of designing NRs@PDA multifunctional theranostic bioprobes for NIR-II imaging-guided tumor vessel tracking and PTT of tumor.

the cell viability was still maintained at above 87 % when treated with the high concentration (1 mg/mL) of the NRs@PDA, indicating the low cytotoxicity of $NaLuF_4$ NRs@PDA. In view of the good biocompatibility and excellent NIR-II emission of NRs@PDA, *in vivo* NIR-II imaging of the anesthetized mouse intravenously injected with the NRs@PDA solution was performed by using 1525 nm emission. As shown in **Figure 2A** and **2B**, the time-dependent *in vivo* whole-body vessel imaging of lewis lung cancer (LLC) tumor-bearing and normal mouse was achieved. A strong NIR-II fluorescent signal from vessel can be detected at 30 s post-injection. And the signal in vessel decreased with increasing the post-injection time and almost disappeared after 20 min injection. It is noted that the distribution and size of the blood vessels are different in tumor-bearing and normal mice (marked with dashed box). The size of blood vessel in tumor-bearing mouse was bigger than that in normal mouse. To further reveal the difference, the corresponding zoom-in images of the chosen zones were demonstrated (**Figure 2C** and **2E**) and the intensity profiles along the line perpendicular to the tumor and normal vessel were shown in **Figure 2D** and **2F**. The vessel widths were evaluated based on the corresponding full width at half-maximum (FWHM) of the peaks according to the Gaussian fitting method. The vessel width obtained from tumor-bearing mouse (0.68 mm) was significantly larger than that of normal vessel (0.49 mm), suggesting the identification of the neovascular and detection of the abnormalities of blood vessels. And the time-dependent signal intensity changes in the heart and liver site of the tumor-bearing mouse were recorded. The signal in heart was decreased while the signal of liver was increased with prolonging injection time, indicating the real-time translocation of nanoprobes from systemic circulation to liver (**Figure S8**). And the average fluorescence intensity ratio between the liver and tumor was evaluated to be 3.28 after 60 h injection (**Figure S9**).

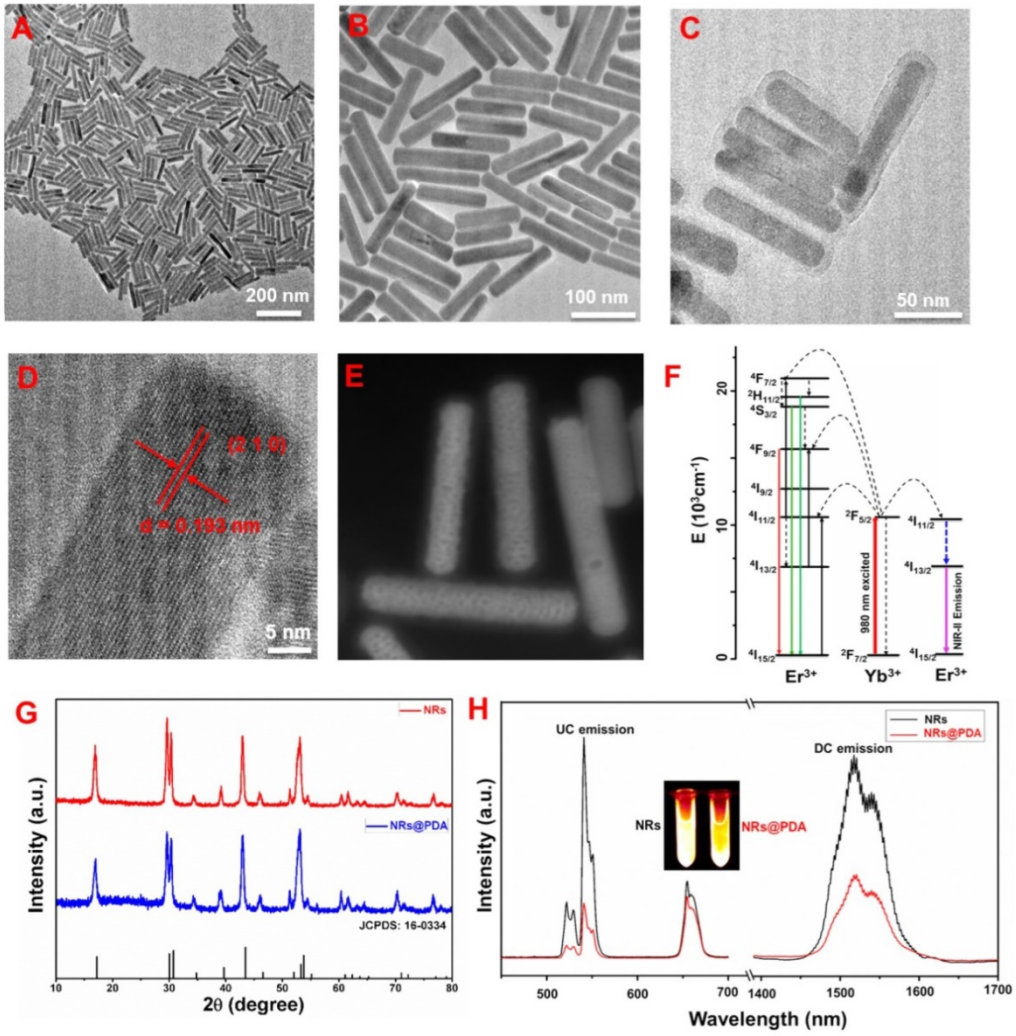

Figure 1. TEM images of the $NaLuF_4$: Gd/Yb/Er NRs: (A) low magnification and (B) high magnification. (C) TEM image of NRs@PDA nanocomposites. (D) HR-TEM image of a single $NaLuF_4$ NR. (E) STEM image of $NaLuF_4$ NRs@PDA. (F) Simplified energy level diagram revealing the energy transfer between Yb^{3+} and Er^{3+}. (G) XRD patterns of $NaLuF_4$ NRs and NRs@PDA. (H) UC and DC luminescence spectra of $NaLuF_4$ NRs and NRs@PDA.

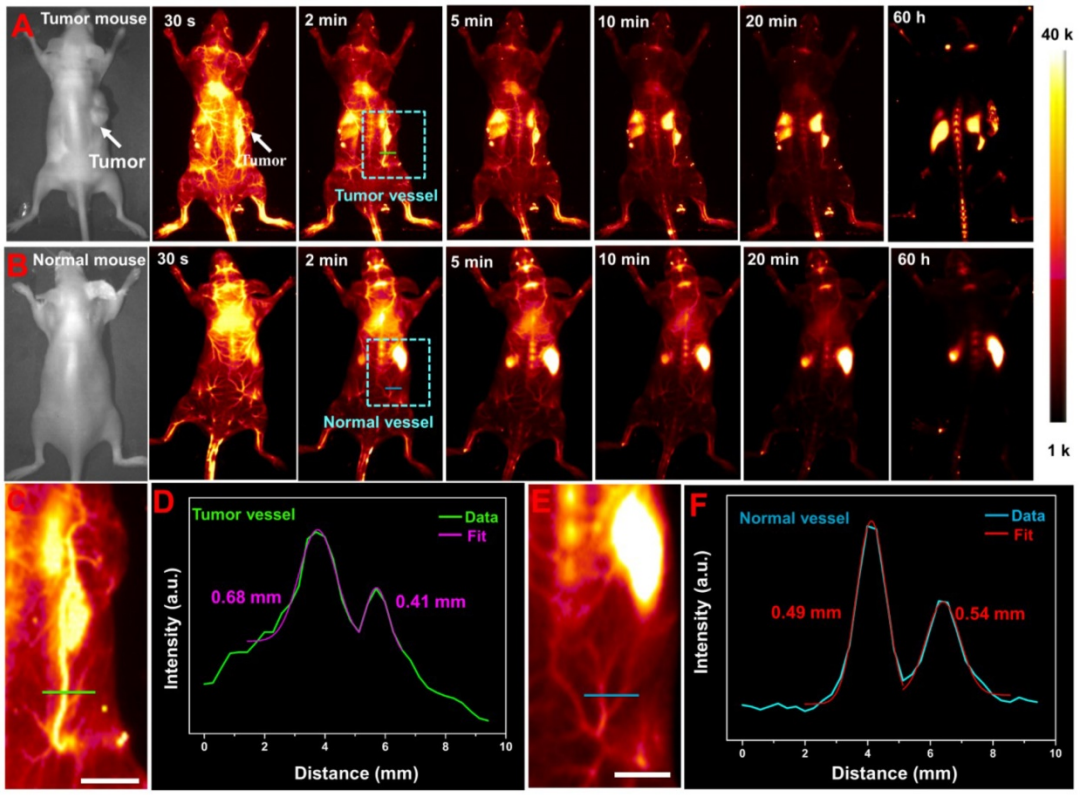

Figure 2. NIR-II imaging guided tumor vessel tracking and whole-body vessel imaging: (A) LLC tumor-bearing mouse. (B) Normal mouse. (C) and (E) The corresponding zoom-in images of the chosen vessels taken from the rectangle in (A) and (B), respectively. (D) Cross-sectional NIR-II intensity profiles along a green line in tumor-bearing mouse. (F) Cross-sectional NIR-II intensity profiles along a blue line in normal mouse. All scale bars are 10 mm.

Additionally, *ex vivo* NIR-II optical bioimaging of the isolated organs (liver, heart, spleen, kidneys, and lung) harvested from the mouse were carried out under 980 nm laser excitation. As demonstrated in **Figure S10**, no obvious optical signal can be observed in heart and kidney, while bright NIR-II signal can be detected in both liver and spleen and dramatically decreased after 7 days injection, implying the main hepatic excretion route of NRs@PDA nanoprobes in living mouse. Moreover, the pharmacokinetic profiles (**Figure S11A**) of $NaLuF_4$ NRs@PDA in living mouse were also evaluated by measuring the blood samples [54] at various time points and the half-life of this probe in blood circulation was measured to be ~72 min. And the *ex vivo* imaging of the feces (**Figure S11B**) further demonstrated the main hepatic excretion of NRs@PDA nanoprobes. In addition, the high magnification NIR-II bioimaging of tumor site with field of view (FOV) of 26 mm × 21 mm was performed (**Figure S12**). As shown in **Figure S12A**, after intravenous injection with NRs@PDA solution, an obvious large-sized blood vessel connecting to the tumor site and abundant small vessels around and in the tumor site were clearly observed, which may provide necessary conditions for the tumor growth. The corresponding vessel widths along the colour lines marked in **Figure S12A** were evaluated to be 304.42 μm (**Figure S12B**) and 120.19 μm (**Figure S12C**) by Gaussian-fitted method.

To further confirm the feasibility of NRs@PDA as optical bioprobes for tumor angiography and vascular abnormalities detection, the low and high magnification NIR-II vessel imaging of another kind of tumor-bearing mouse (colon cancer, HCT-116) were also performed. As shown in **Figure 3E** and **3F**, after intravenous injection with NRs@PDA solution, a single vessel with relative large size was detected and connected to the tumor tissue, further revealing the vascular anomaly for tumor growth. Moreover, the large amount of small vessels in tumor were also observed. And the corresponding vessel widths along the colour lines marked in **Figure 3G** were evaluated to be 312.37, 115.25, 166.32, and 141.25 μm (**Figure 3H**) by Gaussian-fitted method. These findings reveal that the designed NIR-II emissive NRs@PDA are promising NIR-II emitter for whole-body vessel imaging, vascular malformation diagnosis and tumor vessel detection.

Non-invasive brain and abdomen vessel imaging

In vivo non-invasive brain vessel imaging with high spatial resolution has provided an indispensable way to diagnose the cerebral dysfunction or

cerebrovascular diseases. The non-invasive NIR-II optical imaging of mouse's brain was performed by intravenous injection with 200 μL of NRs@PDA solution into an anesthetic nude mouse by a home-made *in vivo* imaging system equipped with InGaAs detector (NIRvana™ Camera System, Princeton Instruments) under 980 nm laser excitation. As shown in **Figure 4A**, the main venule vessels of the mouse brain can be obviously visualized. And the inferior cerebral vein, superior sagittal sinus, and transverse sinus depths (marked by 1, 2, and 3 in **Figure 4A**) under the scalp skin are also visualized. Moreover, many tiny capillary vessels can also be distinguished, indicating the high spatial resolution brain vessel imaging. Therefore, the synthesized NRs@PDA nanoprobes can be utilized as fluorescent agents for non-invasive cerebral vascular imaging through scalp and skull without craniotomy. To further study the vascular bifurcations, the intensity profiles of the vessels marked in **Figure 4B** were studied. The corresponding zoom-in images of the chosen zones were exhibited in **Figure 4C** and **4D**. Due to the inevitable scattering and absorbance from the biotissues, the FWHM was used to represent the vessel's diameter. As demonstrated in **Figure 4E** and **4F**, the vessel widths were measured to be 45.15 and 85.45 μm. These results indicated that the designed NRs@PDA nanocomposites were ideal probes for brain blood vessel imaging.

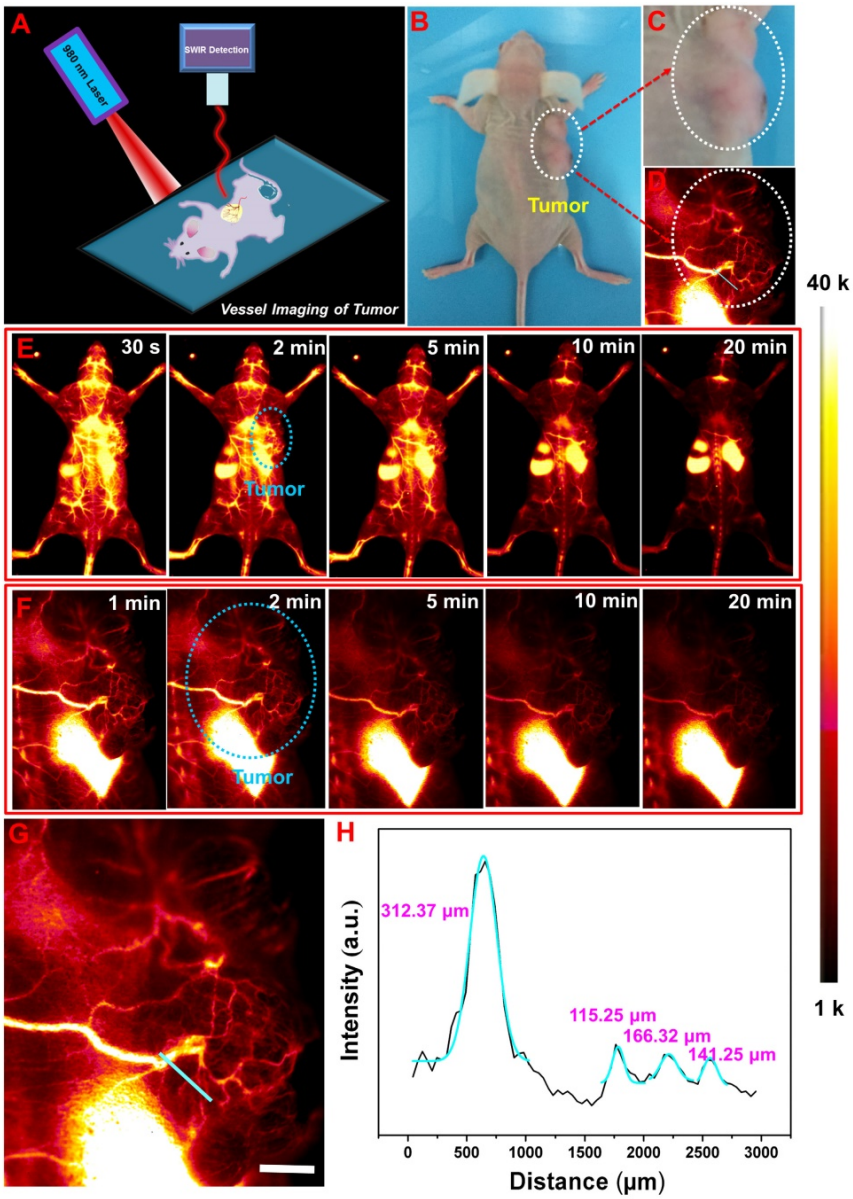

Figure 3. (A) Schematic illustration of non-invasive NIR-II imaging-guided tumor vessel diagnosis. (B) A digital photograph of the tumor-bearing mouse (HCT-116). (C) Bright field image and (D) NIR-II imaging of tumor. The time course of low-magnification (E) and high-magnification (F) tumor vascular imaging. (G) The zoom-in image of the chosen vessels marked by cyan circle in (F). (H) Cross-sectional intensity profiles along the colour lines marked in (G). The scale bar is 2 mm.

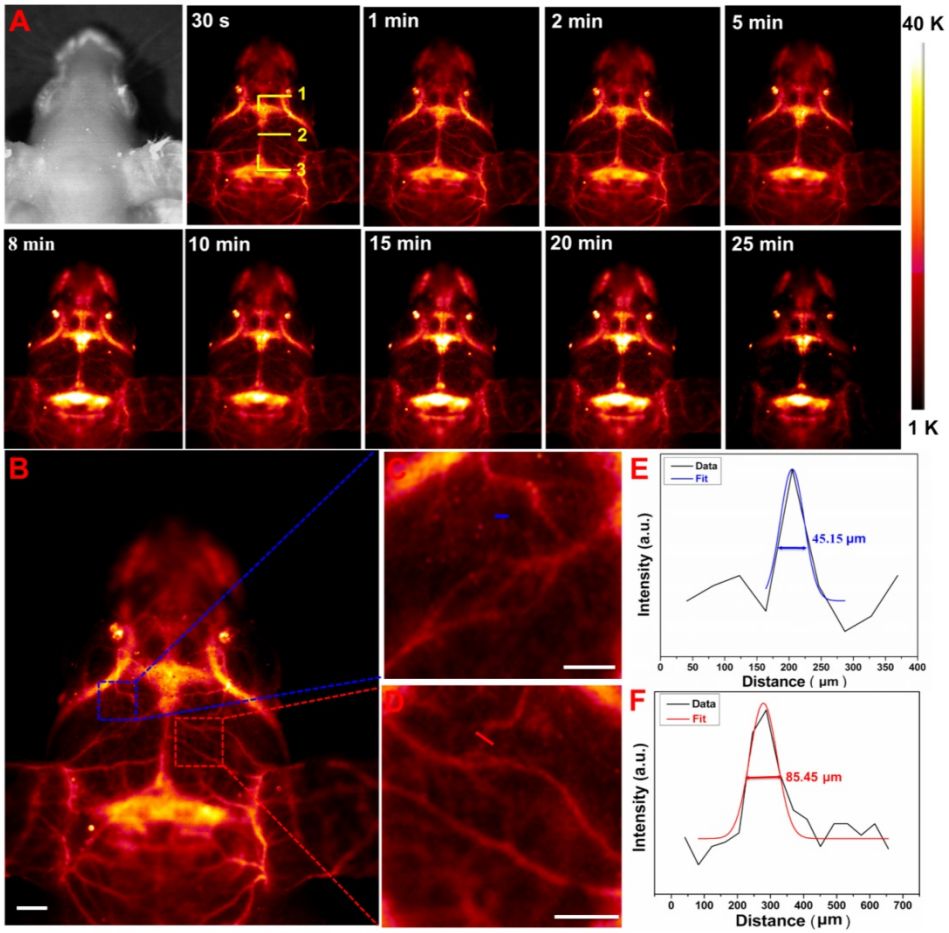

Figure 4. (A) Time-dependent non-invasive *in vivo* brain vessel imaging; 1, 2 and 3 marked in (A) present the inferior cerebral vein, superior sagittal sinus and transverse sinus depths, respectively. (B) A cerebral vascular image. (C) and (D) The corresponding zoom-in images of the chosen vessels. (E) and (F) Cross-sectional intensity profiles (black curves), Gaussian function fitting lines (colorized curves) and FWHM values measured along the colorized lines from the images of (C) and (D). Scale bars: 2 mm.

To further test the feasibility of high resolution blood vessel imaging, the abdominal vessel imaging was also performed. As shown in the Supplementary **Figure S13**, the abdomen blood vessels were also identified with high resolution. Small vessels with diameters of 58.41 and 125.23 μm measured by the Gaussian-fitting method were achieved. These findings validate that our developed NRs@PDA nanocomposites are promising probes for non-invasive high spatial resolution blood vessel imaging.

In vitro photothermal performance and PTT of tumor

To reveal the potential ability of utilizing NRs@PDA in PTT application, we first measured the absorbance spectrum of the samples. As shown in **Figure 5A**, the UV-Vis-NIR absorption spectrum of the NRs@PDA nanoprobes exhibits a broad absorbance from UV to NIR region, making it suitable for PTT application. Furthermore, concentration dependent temperature changes of NRs@PDA solutions were tested. As shown in **Figure 5B**, compared with the ignored temperature increase of the pure water, the NRs@PDA solution (0.2 mg/mL) presents a remarkable temperature increase from 19.8 °C to 53.8 °C under the irradiation of 808 nm laser (3 W/cm^2) for 600 s, which is also vividly visualized in photothermal pictures (**Figure S14**). To further investigate the photothermal performance of the NRs@PDA nanoprobes, the power-dependent temperature changes (**Figure 5C**) of the NRs@PDA solutions were demonstrated. Moreover, the photothermal stability of the NRs@PDA nanoprobes was evaluated by four heating-cooling cycles (**Figure 5D**) through turning on/off laser, indicating the high photothermal-stability of the NRs@PDA nanoprobes. Photothermal conversion efficiency (η) of NRs@PDA nanocomposites was calculated to be 40.18% by using the fitting value of the cooling time versus negative natural logarithm data (**Figure 5F**), which was obtained from the cooling period curve in **Figure 5E.** The photothermal conversion efficiency was higher than that of Au nanorods (21%) [55] and Cu_9S_5 nanocrystals (25.7%) [56].

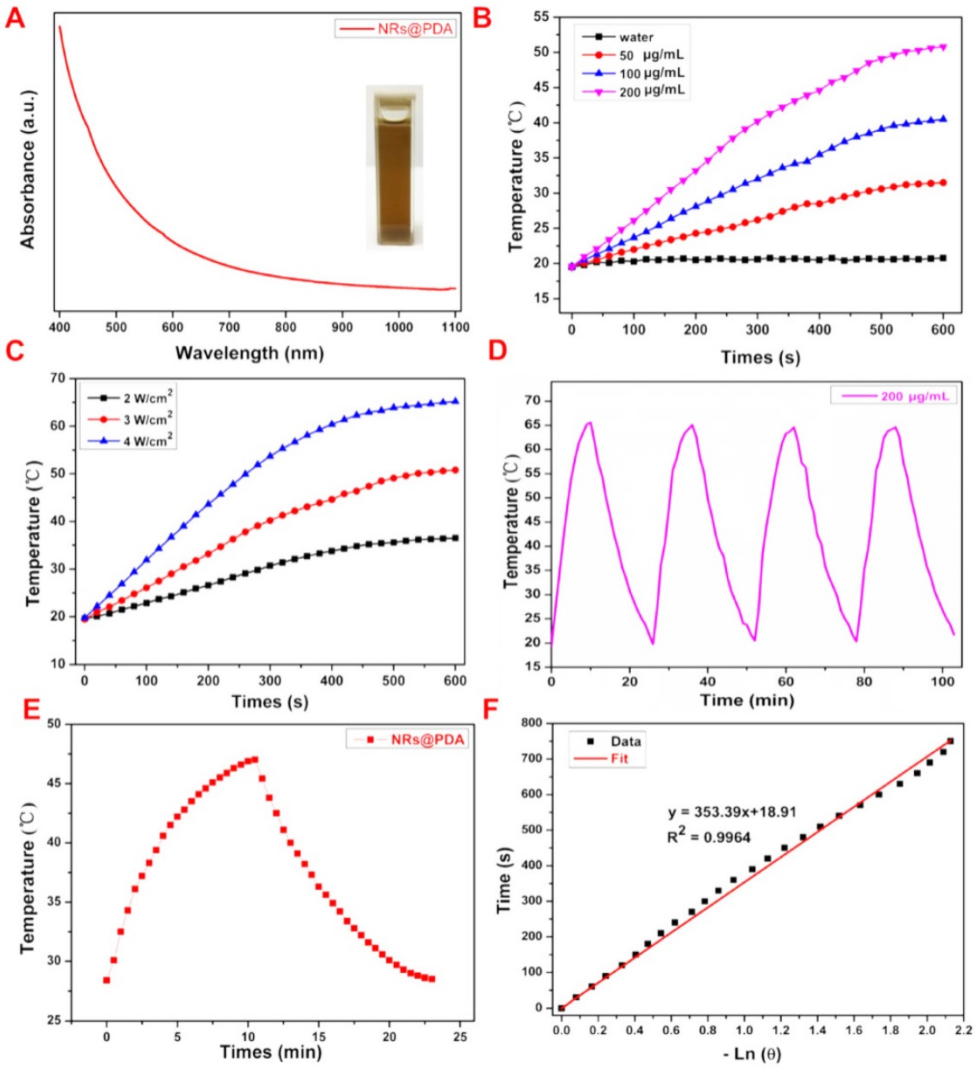

Figure 5. (A) The UV-vis-NIR absorption spectrum of the NRs@PDA solution and the corresponding photograph (the inset). (B) Temperature variation curves of NRs@PDA solutions with different concentrations recorded under 808 nm laser irradiation. (C) Temperature variation curves of NRs@PDA solutions under irradiation with different powers of 808 nm laser. (D) Temperature change of NRs@PDA solutions under four heating/cooling cycles. (E) The photothermal response of the NRs@PDA solution with laser and then the laser was ceased for naturally cooling. (F) Cooling time versus negative natural logarithm of driving force temperature obtained from the cooling stage of (E).

Due to the high photothermal performance of NRs@PDA nanoprobes *in vitro*, *in vivo* photothermal properties and PTT of tumor were studied. To demonstrate the thermal effect of NRs@PDA *in vivo*, mice were subcutaneously injected with phosphate buffer saline (PBS) and NRs@PDA and irradiated with 808 nm laser for 10 min. As shown in **Figure 6A**, in contrast to the PBS group, the temperature of the mouse injected with NRs@PDA was significantly increased to ~55 °C. Therefore, the NRs@PDA nanoprobe could serve as an effective PTT agent for tumor ablation by irradiation with 808 nm laser. Then, the LLC tumor-bearing nude mice were used to evaluate the therapeutic efficacy. The tumor-bearing mice were randomly divided into four groups and treated with PBS, NRs@PDA, NIR irradiation (as control) and NRs@PDA + NIR irradiation. The tumor mice were treated with the 808 nm laser for 10 min every day. The change of tumor size was recorded after treatment (**Figure 6C** and **6B**). As demonstrated, the control groups showed rapid tumor growth and possessed large size, while mice treated with NRs@PDA and 808 nm laser irradiation presented remarkable inhibition of tumor growth, indicating the efficient tumor ablation by PTT. It is expected that the developed NRs@PDA nanoprobes with high photothermal conversion efficiency are promising theranostic agents for *in vivo* PTT of cancer.

Histological analysis

The bioprobes with excellent biocompatibility are highly demanded for biomedicine applications. The toxicity of NRs@PDA in living mouse was tested by a commonly used histological assessment method. **Figure S15** shows the histological analysis results of the main organs (heart, liver, spleen, lung and kidney) of treated groups and control group mouse stained

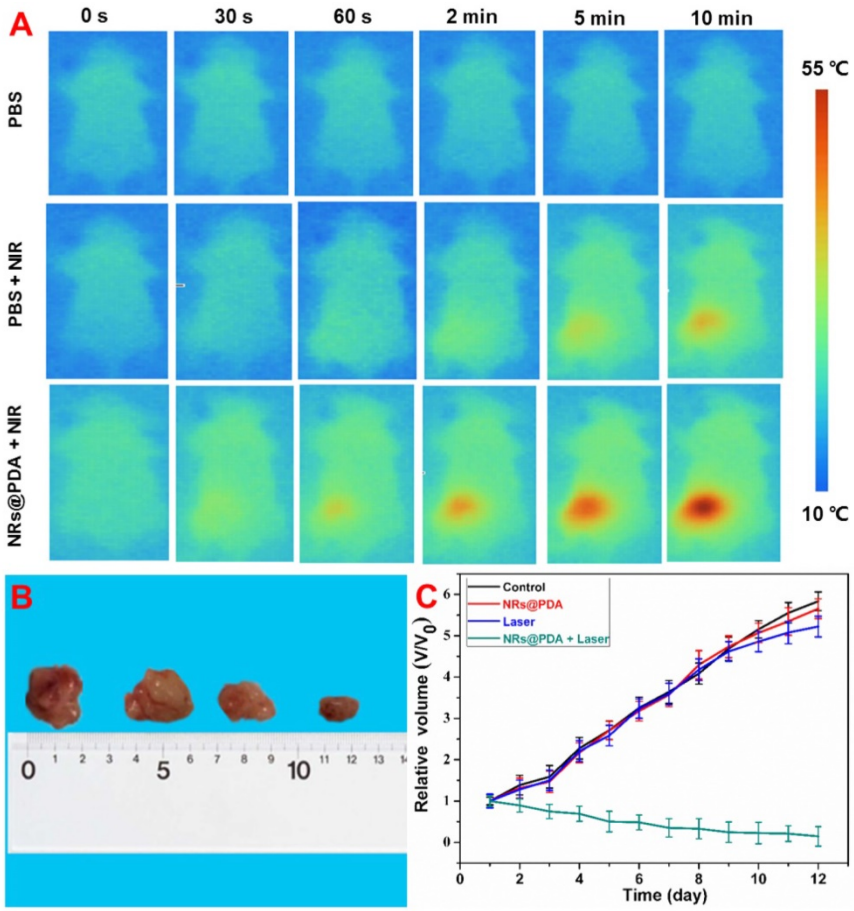

Figure 6. (A) *In vivo* photothermal imaging of mice subcutaneous injection with PBS and NRs@PDA solution under the irradiation of 808 nm laser. (B) The photographs of dissected tumor from the different groups of tumor mice at the end of PTT time. (C) Relative tumor volume after treatment with PBS, NRs@PDA, Laser (control) and NRs@PDA + 808 nm Laser irradiation.

with hematoxylin and eosin (H&E). No apparent lesions in the isolated organs were observed, indicating the good biocompatibility and negligible toxicity of the NRs@PDA for biomedical application.

Conclusions

In summary, the core-shell structured $NaLuF_4$: Gd/Yb/Er NRs@PDA therapeutic agents composed of NIR-II emitting core with controlled size and high QY (1.37%) and photothermal shell of PDA were constructed. Non-invasive brain/abdomen vessel imaging with high spatial resolution (45.15 μm) was demonstrated by using this NIR-II bioprobe. More importantly, non-invasive vascular malformation/ tumor vessel imaging was also achieved by using this NRs@PDA probe, indicating the obvious pathological changes of the blood vessels. Apart from the excellent NIR-II bioimaging, the designed NRs@PDA also can be used as highly efficient 808 nm laser-activated PTT agent according to the high photothermal conversion efficiency. And an efficient PTT of LLC tumor-bearing mouse was conducted, revealing the significant inhibition of tumor growth. Therefore, our findings pave the way of designing multifunction theranostic agents by combining the next generation NIR-II optical imaging and PTT into a single system for tumor vessel imaging and imaging-guided tumor ablation.

Methods

Chemicals and materials

All chemical reagents were obtained from the commercial institution and used without further purification. The rare earth (RE) chlorides including $LuCl_3 \cdot 6H_2O$ (99.9%), $GdCl_3 \cdot 6H_2O$ (99.9%), $YbCl_3 \cdot 6H_2O$ (99.9%), and $ErCl_3 \cdot 6H_2O$ (99.9%) were obtained from QingDa elaborate Chemical Reagent Co. Ltd (Shandong). NaOH, NaF, anhydrous alcohol, toluene, oleic acid (OA), IGEPAL CO-520, dopamine hydrochloride, ammonium hydroxide, 1,2-dichloro-ethane (DCE), IR-26 dye, cyclohexane, and other reagents were all purchased from Sinopharm Chemical Reagent Co., China.

Synthesis of $NaLuF_4$: Yb/Er/Gd NRs

$NaLuF_4$: 40%Gd/20%Yb/2%Er NRs were synthesized by a hydrothermal method. In a typical

synthesis route [57], 1.2 g of NaOH was added in 2 mL deionized water with vigorously stirring. 10 mL of anhydrous alcohol and 20 mL of OA were then added to the above solution. A total of 1 mmol of RE (RE=Lu, Gd, Yb, Er) with a designed molar ratio and 8 mL of NaF (1 mol/L) solutions were added into the aforementioned solution under vigorously stirring. Subsequently, the obtained solution was transferred and sealed to a Teflon-lined stainless-steel autoclave after another 30 min stirring and heated at 190 °C for 24 h. The resulting precipitates were separated by centrifugation, washed with ethanol and water three times. The as-synthesized NRs were re-dispersed in cyclohexane and stored at 4 °C for further application.

Preparation of $NaLuF_4$ NRs@PDA

In order to further multifunctional bioapplication, the hydrophilic $NaLuF_4$: Gd/Yb/Er NRs@PDA was obtained by using a previously reported reverse microemulsion method [41]. Typically, 1 g of IGEPAL CO-520 was added into 20 mL of cyclohexane solution containing with $NaLuF_4$: Gd/Yb/Er NRs (30 mg) under vigorously stirred. The mixture was then stirred for 1h. Subsequently, 0.2 mL of ammonium hydroxide (28%) was slowly injected into solution and stirred for another 1 h. After that, 40 mg of dopamine hydrochloride was added into the above solution with ultrasonic treatment for 10 min. Keep the above solution further stirring for 24 h at room temperature and then the NRs@PDA was obtained. Finally the product was precipitated with ethanol and washed with water and ethanol three times. And then the NRs@PDA nanoprobes were re-dispersed in water for further use.

Characterization of $NaLuF_4$ NRs and NRs@PDA

The crystal phase of the synthesized samples was characterized by utilizing a Rigaku D/max 2500 system X-ray diffractometer (XRD) with Cu-Kα radiation (λ = 1.54056 Å) operated at 40 kV and 250 mA. The morphology and size of the samples were characterized by TEM (FEI Tecnai F20) operated at 200 kV. The existed elements in the samples were further determined by XPS equipment (Thermo Fisher Scientific Escalab 250Xi). The FTIR of the surface ligands grafting on the $NaLuF_4$ NRs was detected by a FTIR spectrometer (AVATAR370 FT-2R, Thermo Nicdet) at room temperature. Visible emission spectra of the samples were recorded via a Zolix Analytical Instrument (fluoroSENS 9000 A) and the down-shifting (NIR-II) fluorescence spectra were detected by using a NIR spectrometer (NIRQuest512, Ocean Optics) ranging from 900 to 1700 nm under the excitation of an external 980 nm laser. A UV-Vis-NIR spectrum was recorded with the absorption spectrometer (Lambda750, Perkin-Elmer) at room temperature.

Photothermal performance measurement of NRs@PDA

To illustrate the photothermal conversion performance of NRs@PDA naoprobes, 2 mL of tube containing with aqueous dispersion of NRs@PDA nanocomposites (0.15 mg/mL) was irradiated with 808 nm laser at 3 W cm^{-2} for 10 min and cooled down for 15 min. And, the temperature change curve was monitored by infrared thermal camera (Ti95, FLUKE). The photothermal conversion efficiency (η) of NRs@PDA was calculated according to the following formula [41]:

$$\eta = \frac{hA(T_{\max} - T_{sur}) - Q_0}{I\left(1 - 10^{-A_{\lambda 808}}\right)}$$

where h represents the heat transfer coefficient, A denotes the surface area of the container, T_{max} and T_{sur} are the equilibrium temperature and ambient temperature, respectively. Q_0 represents the heat dissipation from the light absorbed by container, I is the incident laser power, and $A_{\lambda 808}$ is the absorption intensity of NRs@PDA at 808 nm. The value of hA is derived according to the following equation:

$$hA = \left(\sum m_i c_{p,i}\right) / \tau_s$$

where τ_S is the sample system time constant, m_i and $C_{p,i}$ are the mass and heat capacity of solvent, respectively. The Q_0 is measured independently using sample cell containing pure water without sample. The value of τ_S is calculated by the cooling curve and following equation:

$$\tau_s = -t / \ln \theta$$

Quantum yield measurement

The fluorescence QY of the $NaLuF_4$ NRs@PDA in water was calculated in a similar way to the reported method using a standard IR-26 dye (dissolved in DCE, QY = 0.5%) as a reference [58]:

$$\phi_s = \phi_r \left(F_S / F_r\right) * \left(A_r / A_s\right) * \left(n_s^2 / n_r^2\right)$$

where Φ represents quantum yield, F denotes the integrated photoluminescence emission intensity, A denotes absorbance at the maximum excitation wavelength and n is the refractive index of the solvent (n = 1.44 for DCE, n = 1.33 for water, respectively). The subscripts s and r represent the sample and reference solutions, respectively.

Tumor animal models

8×10^6 Lewis lung cancer (LLC), and colon (HCT-116) cells were subcutaneously injected into nude mice with further culture to obtain the tumor-bearing mouse models for *in vivo* whole body vascular imaging of tumor mouse, high-magnification tumor vascular imaging and PTT therapy experiments. All animal procedures obeyed the Guidelines for the Care and Use of Laboratory Animals of Hunan Normal University and approved by the Animal Ethics Committee of Hunan Province.

In vitro cytotoxicity assay

The cytotoxicity of the $NaLuF_4$ NRs@PDA was evaluated by using a MTT proliferation assay method. HeLa cells were cultured in a 96-well micro-plate at 37 °C under 5% CO_2. Then, the cell culture medium in each well was added with different concentrations of $NaLuF_4$ NRs@PDA (0, 100, 200, 400, 600, 800, 1000 μg/mL). Subsequently, the cells were incubated for another 24 h in the incubator. Then the cell viability was tested by the MTT method.

NIR-II optical bioimaging

The *in vivo* optical imaging of nude mouse based on NRs@PDA was captured by using a home-made small animal NIR-II bioimaging system (*In Vivo* Master, Wuhan Grand-imaging Technology Co., LTD) equipped with an InGaAs camera (Model: NIRvana™ Camera System, Default Operating temperature: -80 °C, Princeton Instruments, 512 × 640 pixels) under the excitation of a 980 nm laser with a band pass filter (1400 -1600 nm) [59]. All the whole body imaging in this work was detected by using a NIR-II lens (25 mm, Edmund Optics) with a field of view of 14.6 cm × 18.3 cm. The NRs@PDA (200 μL, 2 mg/mL) probes were intravenously injected into the mouse to acquire NIR-II real-time tracking images under the excitation of 980 nm laser (100 mW/cm², 2 s). The *ex-vivo* bioimaging of the main organs (heart, lung, spleen, liver and kidney) harvested from the treated mice were performed with the same parameters to assess the biodistribution and accumulation of the NRs@PDA in living mice. The digital picture of the tumor was taken by using a Canon digital camera.

The blood half-life time was tested based on the blood fluorescence intensity according to the previous report [54]. The Kunming mice were first intravenously injected with $NaLuF_4$ NRs@PDA (200 μL, 2 mg/mL), the blood samples were collected at time points from 1 min to 24 h. The content of the $NaLuF_4$ NRs@PDA in blood was evaluated by recording the fluorescence intensity under the excitation of 980 nm laser with power density of 100 mW/cm².

High magnification blood vessel imaging based on NRs@PDA in NIR-II region

The high magnification NIR-II blood vessel imaging of mouse brain, abdomen vein and tumor vessels was performed by using the same NIR-II bioimaging system (NIR-II lens: 100 mm, Edmund Optics, FOV: 21 mm × 26 mm, 512 × 640 pixels, 41 μm/pixel) by intravenously injecting with NRs@PDA solution into the anesthetized nude mice under the excitation of 980 nm laser (100 mW/cm², 2s).

In vitro and *in vivo* PTT treatment of tumor mouse

For *in vitro* photothermal properties evaluation, the $NaLuF_4$ NRs@PDA solutions with different concentrations (0, 0.05, 0.1, 0.2 mg/mL) were irradiated by NIR laser exposure (808 nm, 3 W/cm²) in 2 mL test tubes. And, the power-dependent temperature change of the NRs@PDA solution and the temperature change curves were also detected. In addition, the photothermal stability of the NRs@PDA solution was also investigated by continuous 10 min irradiation, cooling to room temperature, and followed by another 10 min irradiation for four cycles.

For *in vivo* photothermal evaluation, the normal mice were randomly divided into three groups (Group 1: subcutaneous injection with PBS (as control); Group 2: subcutaneous injection with PBS + 808 nm laser irradiation; Group 3: subcutaneous injection with NRs@PDA solution (0.2 mL, 0.2 mg/mL) + 808 nm laser irradiation). The *in vivo* temperature changes of the treated mice were recorded by FLUKE thermal camera under the 808 nm laser irradiation for 10 min. Then, the LLC tumor-bearing mice were divided to four groups for PTT experiments. And the tumor-bearing mice were treated with 808 nm laser irradiation for 10 min every day. The tumor sizes of each group were measured after post-treatment.

Histology analysis

To evaluate *in vivo* toxicity of $NaLuF_4$ NRs@PDA, the histological tests of the major organs including heart, liver, spleen, lung and kidney with hematoxylin and eosin (H&E) staining obtained from the control and test (after 3 and 7 days of injection) groups were performed. The Kunming mice injected with 0.2 mL of $NaLuF_4$ NRs@PDA (2 mg/mL) were denoted as the test group. The untreated mice were selected as control group.

Abbreviations

NRs: nanorods; PDA: polydopamine; NIR: near-infrared; NIR-II: second near-infrared; PTT: photothermal therapy; NIR-I: first near-infrared; QDs:

quantum dots; SWNTs: single-walled carbon nanotubes; QY: quantum yield; TEM: transmission electron microscopy; HR-TEM: high resolution TEM; STEM: scanning transmission electron microscope; XRD: X-ray diffraction; XPS: X-ray photoelectron spectroscopy; FTIR: Fourier transform infrared; UC: upconversion; DC: downconversion; FRET: fluorescence resonance energy transfer; MTT: 3-(4, 5-dimethylthiazol-2-yl)-2-5-diphenyl-tetrazolium bromide; ICG: indocyanine green; FWHM: full width at half-maximum; FOW: field of view; LLC: Lewis lung cancer; PBS: phosphate buffer saline; H&E: hematoxylin and eosin.

Supplementary Material

Supplementary figures.
http://www.thno.org/v09p3866s1.pdf

Acknowledgments

This work was supported by the National Natural Science Foundation of China (Nos. 31570742, 21671064), Natural Science Foundation of Hunan Province, China (2019JJ10002), Science and Technology Planning Project of Hunan Province (Nos. 2017RS3031, 2017RS3033), and the Hunan Provincial Innovation Foundation for Postgraduate (CX2017B223).

Competing Interests

The authors have declared that no competing interest exists.

References

1. He F, Yang GX, Yang PP, Yu YX, Lv RC, Li CX, et al. A new single 808 nm NIR light-induced imaging-guided multifunctional cancer therapy platform. Adv Funct Mater. 2015; 25: 3966-76.
2. Wang YH, Wang HG, Liu DP, Song SY, Wang X, Zhang HJ. Graphene oxide covalently grafted upconversion nanoparticles for combined NIR mediated imaging and photothermal/photodynamic cancer therapy. Biomaterials. 2013; 34: 7715-24.
3. Cheng L, Yang K, Li YG, Chen JH, Wang C, Shao MW, et al. Facile preparation of multifunctional upconversion nanoprobes for multimodal imaging and dual-targeted photothermal therapy. Angew Chem Int Ed Engl. 2011; 50: 7385-90.
4. Xiao QF, Zheng XP, Bu WB, Ge WQ, Zhang SJ, Chen F, et al. A core/satellite multifunctional nanotheranostic for *in vivo* imaging and tumor eradication by radiation/photothermal synergistic therapy. J Am Chem Soc. 2013; 135: 13041-8.
5. Dong K, Liu Z, Li ZH, Ren JS, Qu XG. Hydrophobic anticancer drug delivery by a 980 nm laser-driven photothermal vehicle for efficient synergistic therapy of cancer cells *in vivo*. Adv Mater. 2013; 25: 4452-8.
6. Ding XG, Liow CH, Zhang MX, Huang RJ, Li CY, Shen H, et al. Surface plasmon resonance enhanced light absorption and photothermal therapy in the second near-infrared window. J Am Chem Soc. 2014; 136: 15684-93.
7. Dong H, Du SR, Zheng XY, Lyu GM, Sun LD, Li LD, et al. Lanthanide nanoparticles: from design toward bioimaging and therapy. Chem Rev. 2015; 115: 10725-815.
8. Xu JT, Gulzar A, Liu YH, Bi HT, Gai SL, Liu B, et al. Integration of IR-808 sensitized upconversion nanostructure and MoS_2 nanosheet for 808 nm NIR light triggered phototherapy and bioimaging. Small. 2017; 13: 1701841.
9. Li S, Xu LG, Sun MZ, Wu XL, Liu LQ, Kuang H, et al. Hybrid nanoparticle pyramids for intracellular dual microRNAs biosensing and bioimaging. Adv Mater. 2017; 29: 1606086.
10. Liu YX, Fan HM, Guo QW, Jiang AQ, Du XX, Zhou J. Ultra-small pH-responsive Nd-doped $NaDyF_4$ Nanoagents for enhanced cancer theranostic by in situ aggregation. Theranostics. 2017; 7: 4217-28.
11. Wang ZH, Ma Y, Yu XY, Niu Q, Han ZH, Wang H, et al. Targeting CXCR4–CXCL12 axis for visualizing, predicting, and inhibiting breast cancer metastasis with theranostic AMD3100–Ag_2S quantum dot probe. Adv Funct Mater. 2018; 28: 1800732.
12. Song XR, Wang XY, Yu SX, Cao JB, Li SH, Li J, et al. Co_9Se_8 Nanoplates as a new theranostic platform for photoacoustic/magnetic resonance dual-modal-imaging-guided chemo-photothermal combination therapy. Adv Mater. 2015; 27: 3285-91.
13. Song GS, Liang C, Gong H, Li MF, Zheng XC, Cheng L, et al. Core–shell MnSe@Bi_2Se_3 fabricated via a cation exchange method as novel nanotheranostics for multimodal imaging and synergistic thermoradiotherapy. Adv Mater. 2015; 27: 6110-7.
14. Cui SS, Yin DY, Chen YQ, Di YF, Chen HY, Ma YX, et al. *In vivo* targeted deep-tissue photodynamic therapy based on near-infrared light triggered upconversion nanoconstruct. ACS Nano. 2013; 7: 676-88.
15. Yang D, Yang GX, Yang PP, Lv RC, Gai SL, Li CX, et al. Assembly of Au plasmonic photothermal agent and iron oxide nanoparticles on ultrathin black phosphorus for targeted photothermal and photodynamic cancer therapy. Adv Funct Mater. 2017; 27: 1700371.
16. Zhang Y, Cui ZF, Kong HT, Xia K, Pan L, Li J, et al. One-shot immunomodulatory nanodiamond agents for cancer immunotherapy. Adv Mater. 2016; 28: 2699-708.
17. Wang XD, Pang YJ, Ku G, Ku XY, Stoica G, Wang LHV. Noninvasive laser-induced photoacoustic tomography for structural and functional *in vivo* imaging of the brain. Nat Biotechnol. 2003; 21: 803-6.
18. Hong GS, Diao S, Chang JL, Antaris AL, Chen CX, Zhang B, et al. Through-skull fluorescence imaging of the brain in a new near-infrared window. Nat Photonics. 2014; 8: 723-30.
19. Vijayaraghavan P, Vankayala R, Chiang CS, Sung HW, Hwang KC. Complete destruction of deep-tissue buried tumors via combination of gene silencing and gold nanoechinus-mediated photodynamic therapy. Biomaterials. 2015; 62: 13-23.
20. Yi ZG, Li XL, Xue ZL, Liang X, Lu W, Peng H, et al. Remarkable NIR enhancement of multifunctional nanoprobes for *in vivo* trimodal bioimaging and upconversion optical/T_2-weighted MRI-guided small tumor diagnosis. Adv Funct Mater. 2015; 25: 7119-29.
21. Zhu SJ, Yung BC, Chandra S, Niu G, Antaris AL, Chen XY. Near-infrared-II (NIR-II) bioimaging via off-peak NIR-I fluorescence emission. Theranostics. 2018; 8: 4141-51.
22. Zhu SJ, Hu ZB, Tian R, Yung BC, Yang QL, Zhao S, et al. Repurposing cyanine NIR-I dyes accelerates clinical translation of near-infrared-II (NIR-II) bioimaging. Adv Mater. 2018; 30: 1802546.
23. Tao ZM, Hong GS, Shinji C, Chen CX, Diao S, Antaris AL, et al. Biological imaging using nanoparticles of small organic molecules with fluorescence emission at wavelengths longer than 1000 nm. Angew Chem Int Ed Engl. 2013; 52: 13002-6.
24. Antaris AL, Chen H, Diao S, Ma ZR, Zhang Z, Zhu SJ, et al. A high quantum yield molecule-protein complex fluorophore for near-infrared II imaging. Nat Commun. 2017; 8: 15269.
25. Zhang Y, Hong GS, Zhang YJ, Chen GC, Li F, Dai HJ, et al. Ag_2S quantum dot: a bright and biocompatible fluorescent nanoprobe in the second near-infrared window. ACS Nano. 2012; 6: 3695-702.
26. Hong GS, Robinson JT, Zhang YJ, Diao S, Antaris AL, Wang QB, et al. *In vivo* fluorescence imaging with Ag_2S quantum dots in the second near-infrared region. Angew Chem Int Ed Engl. 2012; 51: 9818-21.
27. Welsher K, Liu Z, Sherlock SP, Robinson JT, Chen Z, Daranciang D, et al. A route to brightly fluorescent carbon nanotubes for near-infrared imaging in mice. Nat Nanotechnol. 2009; 4: 773-80.
28. Robinson JT, Hong GS, Liang YY, Zhang B, Yaghi OK, Dai HJ. *In vivo* fluorescence imaging in the second near-infrared window with long circulating carbon nanotubes capable of ultrahigh tumor uptake. J Am Chem Soc. 2012; 134: 10664-9.
29. Hong GS, Zou YP, Antaris AL, Diao S, Wu D, Cheng K, et al. Ultrafast fluorescence imaging *in vivo* with conjugated polymer fluorophores in the second near-infrared window. Nat Commun. 2014; 5: 4206.
30. Huang S, Upputuri PK, Liu H, Pramanik M, Wang MF. A dual-functional benzobisthiadiazole derivative as an effective theranostic agent for near-infrared photoacoustic imaging and photothermal therapy. J Mater Chem B. 2016; 4: 1696-703.
31. Rogach AL, Eychmuller A, Hickey SG, Kershaw SV. Infrared-emitting colloidal nanocrystals: synthesis, assembly, spectroscopy, and applications. Small. 2007; 3: 536-57.
32. Chen J, Kong YK, Fang HW, Wo Y, Zhou DJ, Wu ZY, et al. Direct water-phase synthesis of lead sulfide quantum dots encapsulated by β-lactoglobulin for *in vivo* second near infrared window imaging with reduced toxicity. Chem Commun. 2016; 52: 4025-8.
33. Dong BH, Li CY, Chen CC, Zhang YJ, Zhang Y, Deng MJ, et al. Facile synthesis of highly photoluminescent Ag_2Se quantum dots as a new fluorescent probe in the second near-infrared window for *in vivo* imaging. Chem Mater. 2013; 25: 2503-9.
34. Bakueva L, Gorelikov I, Musikhin S, Zhao XS, Sargent EH, Kumacheva E. PbS quantum dots with stable efficient luminescence in the near-IR spectral range. Adv Mater. 2004; 16: 926-9.

35. Liu Z, Cai WB, He LN, Nakayama N, Chen K, Sun XM, et al. *In vivo* biodistribution and highly efficient tumour targeting of carbon nanotubes in mice. Nat Nanotechnol. 2006; 2: 47-52.
36. Welsher K, Liu Z, Daranciang D, Dai HJ. Selective probing and imaging of cells with single walled carbon nanotubes as near-infrared fluorescent molecules. Nano Lett. 2008; 2: 586-90.
37. Villa I, Vedda A, Cantarelli IX, Pedroni M, Piccinelli F, Bettinelli M, et al. 1.3 μm emitting SrF_2: Nd^{3+} nanoparticles for high contrast *in vivo* imaging in the second biological window. Nano Res. 2015; 8: 649-65.
38. Naczynski DJ, Tan MC, Zevon M, Wall B, Kohl J, Kulesa A, et al. Rare-earth-doped biological composites as *in vivo* shortwave infrared reporters. Nat Commun. 2013; 4: 2199.
39. Robinson JT, Tabakman SM, Liang YY, Wang HL. Casalongue HS, Vinh D, et al. Ultrasmall reduced graphene oxide with high near-infrared absorbance for photothermal therapy. J Am Chem Soc. 2011; 133: 6825-31.
40. Cheng L, Wang C, Feng LZ, Yang K, Liu Z. Functional nanomaterials for phototherapies of cancer. Chem Rev. 2014; 114: 10869-939.
41. Dai Y, Yang DP, Yu DP, Cao C, Wang QH, Xie SH, et al. Mussel-inspired polydopamine-coated lanthanide nanoparticles for NIR-II/CT dual imaging and photothermal therapy. ACS Appl Mater Interfaces. 2017; 9: 26674-83.
42. Ding X, Liu JH, Liu DP, Li JQ, Wang F, Li LJ, et al. Multifunctional core/satellite polydopamine@Nd^{3+}-sensitized upconversion nanocomposite: A single 808 nm near-infrared light-triggered theranostic platform for *in vivo* imaging-guided photothermal therapy. Nano Res. 2017; 10: 3434-46.
43. Ke HT, Wang JR, Dai ZF, Jin YS, Qu EZ, Xing ZW, et al. Gold-nanoshelled microcapsules: a theranostic agent for ultrasound contrast imaging and photothermal therapy. Angew Chem Int Ed Engl. 2011; 50: 3017-21.
44. Tian QW, Tang MH, Sun YG, Zou RJ, Chen ZG, Zhu MF, et al. Hydrophilic flower-like CuS superstructures as an efficient 980 nm laser-driven photothermal agent for ablation of cancer cells. Adv Funct Mater. 2011; 23: 3542-7.
45. Yang K, Zhang S, Zhang GX, Sun XM, Lee ST, Liu Z. Graphene in mice: ultrahigh *in vivo* tumor uptake and efficient photothermal therapy. Nano Lett. 2010; 10: 3318-23.
46. Menon JU, Jadeja P, Tembe P, Vu K, Yuan BH, Nguyen KT. Nanomaterials for photo-based diagnostic and therapeutic applications. Theranostics. 2013; 3: 152-66.
47. Liu YL, Ai KL, Liu JH, Deng M, He YY, Lu LH. Dopamine-melanin colloidal nanospheres: an efficient near-infrared photothermal therapeutic agent for *in vivo* cancer therapy. Adv Mater. 2013; 25: 1353-9.
48. Chen Y, Ai KL, Liu JH, Ren XY, Jiang CH, Lu LH. Polydopamine-based coordination nanocomplex for T_1/T_2 dual mode magnetic resonance imaging-guided chemo-photothermal synergistic therapy. Biomaterials. 2016; 77: 198-206.
49. Cheng YX, Zhang SP, Kang N, Huang JP, Lv XL, Wen K, et al. Polydopamine-coated manganese carbonate nanoparticles for amplified magnetic resonance imaging-guided photothermal therapy. ACS Appl Mater Interfaces. 2017; 9: 19296-306.
50. Ge R, Li X, Lin M, Wang DD, Li SY, Liu SW, et al. Fe_3O_4@polydopamine composite theranostic superparticles employing preassembled Fe_3O_4 nanoparticles as the core. ACS Appl Mater Interfaces. 2016; 8: 22942-52.
51. Wang R, Li XM, Zhou L, Zhang F. Epitaxial seeded growth of rare-earth nanocrystals with efficient 800 nm near-infrared to 1525 nm short-wavelength infrared downconversion photoluminescence for *in vivo* bioimaging. Angew Chem Int Ed Engl. 2014; 53: 12086-90.
52. Hong GS, Antaris AL, Dai HJ. Near-infrared fluorophores for biomedical imaging. Nat Biomed Eng. 2017; 1: 0010.
53. Yi H, Ghosh D, Ham MH, Qi JF, Barone PW, Strano MS, et al. M13 phage-functionalized single-walled carbon nanotubes as nanoprobes for second near-infrared window fluorescence imaging of targeted tumors. Nano Lett. 2012; 12: 1176-83.
54. Zhong YT, Ma ZR, Zhu SJ, Yue JY, Zhang MX, Antaris AL, et al. Boosting the down-shifting luminescence of rare-earth nanocrystals for biologicalImaging beyond 1500 nm. Nat Commun. 2017; 8: 737.
55. Tian QW, Hu JQ, Zhu YH, Zou RJ, Chen ZG, Yang SP, et al. Sub-10 nm Fe_3O_4@$Cu_{2-x}S$ core−shell nanoparticles for dual-modal imaging and photothermal therapy. J Am Chem Soc. 2013; 135: 8571-7.
56. Tian QW, Jiang FR, Zou RJ, Liu Q, Chen ZG, Zhu MF, et al. Hydrophilic Cu_9S_5 nanocrystals: a photothermal agent with a 25.7% heat conversion efficiency for photothermal ablation of cancer cells *in vivo*. ACS Nano. 2011; 5: 9761-71.
57. Zeng SJ, Yi ZG, Lu W, Qian C, Wang HB, Rao L, et al. Simultaneous realization of phase/size manipulation, upconversion luminescence enhancement, and blood vessel imaging in multifunctional nanoprobes through transition metal Mn^{2+} doping. Adv Funct Mater. 2014; 24: 4051-9.
58. Antaris AL, Chen H, Cheng K, Sun Y, Hong GS, Qu CR, et al. A small-molecule dye for NIR-II imaging. Nat Mater. 2016; 15: 235-42.
59. Li YB, Li XL, Xue ZL, Jiang MY, Zeng SJ, Hao JH. Second near-infrared emissive lanthanide complex for fast renal-clearable *in vivo* optical bioimaging and tiny tumor detection. Biomaterials. 2018; 169: 35-44.